Plasma-induced luminescence spectroscopy in Martian atmospheric conditions

Elise Clavé, David Vogt, Susanne Schröder, Sylvestre Maurice, Bruno Bousquet

Version of Record: https://www.sciencedirect.com/science/article/pii/S0584854722001082
Manuscript_0d7eecbc9fce6906483486311e455f18

Plasma-induced luminescence spectroscopy in Martian atmospheric conditions

Elise Clavé[1], David Vogt[2], Susanne Schröder[2], Sylvestre Maurice[3], Bruno Bousquet[1]

[1] Centre Lasers Intenses et applications (CELIA), Université de Bordeaux, CNRS, CEA, Bordeaux, France
[2] Deutsches Zentrum für Luft- und Raumfahrt (DLR), Institute of Optical Sensor Systems, Berlin, Germany
[3] Institut de Recherche en Astrophysique et Planétologie (IRAP), Université de Toulouse 3 Paul Sabatier, CNRS, CNES, Toulouse, France

Keywords: Mars, SuperCam, plasma-induced luminescence, LIBS, time resolution

Abstract

The SuperCam instrument, aboard NASA's Perseverance rover, provides for the first time the hardware capability for time-resolved spectroscopy on Mars. As a consequence, in addition to the atomic and molecular emissions routinely recorded by SuperCam LIBS, plasma-induced luminescence (PIL) features could theoretically also be observed, within the sample, potentially improving the detection capabilities for some minor elements, compared to LIBS. PIL has been studied in terrestrial conditions but not yet examined under Martian atmospheric conditions. Since atmospheric conditions have previously been shown to strongly affect plasma emissions, they may also have a significant influence on PIL. This study aims at assessing the feasibility of PIL spectroscopy in Martian atmospheric conditions. To do so, we investigate the influence of atmospheric pressure and composition on PIL emissions, compared to plasma emissions. We demonstrate that PIL emission can be observed in simulated Martian conditions, despite its lower intensity compared to terrestrial conditions. Moreover, PIL features exhibiting millisecond-range decay have been observed once plasma emissions have decreased significantly; with our experimental conditions, it is achieved with a temporal delay of 200 μs after plasma initiation and a gate of 20 ms. Shorter-lived PIL features have not been observed, possibly due to spectral interference with plasma emissions.

1. Introduction

The Perseverance rover landed in the Jezero crater, Mars on February 18th, 2021. SuperCam [1–4] is one of the remote science instruments in the payload; it enables multi-technique analyses of the Martian surface around the rover. Laser-induced breakdown spectroscopy (LIBS), together with time-resolved Raman and luminescence spectroscopy, provides chemical and mineralogical information for geologic targets located nominally within 1.5 to 7 m from the rover [1]. Visible and infrared reflectance spectroscopy (VISIR), being a passive spectroscopy technique based on excitation by sunlight, can be applied to analyze targets at distances ranging from 1.5 m up to several kilometers. The remote micro-imager (RMI) provides high-resolution context images for the spectroscopy analyses of targets in the whole distance range covered by VISIR. Additionally, a microphone provides data relevant for both atmospheric science and geology, when coupled with LIBS [5].
SuperCam LIBS, Raman and luminescence techniques make use of a pulsed Nd-YAG laser (3-4 ns ; 3-10 Hz ; 9-14 mJ), operating at 1064 nm for LIBS and 532 nm for Raman and luminescence [1]. LIBS

plasma emissions are recorded by three spectrometers [2] covering the following spectral ranges: 243.7 – 345.0 nm, 379.0 – 465.0 nm and 532.0 – 858.8 nm. The spectrometer operating in the last range is used for Raman and luminescence spectroscopy. To extract the low-intensity Raman signal from background or overlapping luminescence emissions, this spectrometer implements signal amplification as well as time resolution, acting on both the delay D to start the acquisition after the laser pulse, and the integration time, referred to as the gate G.

All routine LIBS observations (more than 1000 points analyzed by SuperCam over the first ~300 Martian days of the mission [6]) are acquired with D $\leq 20\ ns$ and G $= 34\ \mu s$. Using the same parameters for all observations enables spectra comparison, classification and chemical quantification [7]. On the other hand, for the first time on Mars, it is possible, with SuperCam, to tune D and G, and thus take advantage of time resolution to observe LIBS-related emissions in the 532.0-858.8 nm range.

Previous studies, in terrestrial atmospheric conditions, showed that time resolution enables the observation of plasma-induced luminescence (PIL) following plasma emission, that is, luminescence emission excited within the sample by the laser-induced plasma [8,9]. Without time resolution capabilities, PIL emissions are generally hidden by plasma emissions, which are typically orders of magnitude more intense. Time resolution thus enables to take advantage of the long lifetimes of some luminescence signatures compared to plasma emissions, by using longer delays and gates, increased gain and possibly more laser shots, to optimize the PIL signal. With short delays, these acquisition parameters would result in saturation of plasma emissions. PIL and plasma emission can in principle also be separated spatially as was proposed in a previous study [10]. To do so, the plasma is created outside the field-of-view of PIL detection, either directly beside the plasma, or several centimeters-away, using a set of optical lenses. With SuperCam, the plasma and sample – and hence the LIBS and PIL signals – would be superimposed in the field-of-view of the instrument, but time resolution could be enough to separate the signals. In theory, in sufficiently large crystals, SuperCam could therefore observe PIL signal on Mars, enabling the detection of minor elements, which are typically below the limit of detection with LIBS, as it is the case for some rare-earth elements [9,11].

Considering that the laser-induced plasma is the excitation source for PIL, and can affect the ability to observe PIL emissions, when the different emissions overlap spectrally and temporally, advanced understanding of the LIBS spectrum is very helpful for efficient observation and exploitation of PIL spectra.

In LIBS, the laser-induced plasma is a transient thermodynamic system characterized by a very complex spatial and-temporal evolution [12–16]. As soon as the plasma is created, it starts expanding and cooling in the surrounding atmosphere. In the early stage of plasma expansion, radiative losses are related to free-free and free-bound transitions, and evidenced by a transient broadband continuum in the LIBS spectrum, which is progressively replaced by atomic emission lines related to excitation/de-excitation processes from ions and neutrals. In some cases, after the plasma has cooled sufficiently, molecules can recombine within the plasma through the recombination of atomic reactants; molecular emission bands can then be observed in the LIBS spectra.

This evolution of the plasma is known to be strongly dependent on the pressure and composition of the ambient gas [17–23]. Atmospheric conditions affect the rate of plasma expansion and hence temperature decay as well as density decrease; the ablated mass, spatial distribution of the species within the plasma and exchanges between plasma and surrounding gas also depend on atmospheric conditions. As a consequence, both intensity and decay rates of continuum, atomic and molecular

emissions are strongly influenced by atmospheric conditions. In particular, on Mars, the atmosphere consists in 6-7 mbar of CO_2 (about 96%), with small amounts of Ar and N_2 [24]. In this environment, LIBS studies showed that atomic emissions are both more intense and longer-lived, whereas continuum emission is reduced in Martian conditions compared to terrestrial conditions [18,25–28]. Molecular emissions have been observed on Mars with the ChemCam instrument on Curiosity [29], associated to halogens, such as fluorine and chlorine, with improved detection and even quantification capabilities compared to atomic emission lines [30–32]. Laboratory studies were also dedicated to studying molecular emissions in Mars-like atmospheric conditions [33–37], with a few studies focused on the specific influence of atmospheric conditions on molecular recombination (eg. [38]). A. De Giacomo & J. Hermann [16] explain that molecular emission requires the plasma temperature to be both low enough for molecules formation, and high enough for electronic excitation to occur, together with a sufficiently high density of reactants. As a consequence, molecular band detection is expected to be significantly affected by the properties of the ambient gas.

In this study, we seek to assess the feasibility of PIL spectroscopy in Martian atmospheric conditions. To do so, we investigate how changing atmospheric pressure and composition, and subsequent changing plasma emissions, affect PIL excitation and emission within the sample, as well as its observation. We observe PIL emissions under simulated Martian atmospheric conditions in both natural and synthesized samples and identify time parameters for optimal observation of long-lived emissions.

2. Material & Methods

2.1. Experimental setup and spectra acquisition

Our laboratory test-bed is equipped with a diode-pumped pulsed Nd: YAG laser (Viron, Lumibird) operating at 1064 nm (6 ns; 10 Hz; 12 mJ). The spot diameter is approximately 200 µm, resulting in a laser fluence on the sample surface of approximately 40 J/cm^2. The laser beam is vertically focused with a 20-cm fused silica plano-convex lens onto the surface of the sample. The resulting emission is collected and then injected into a circle-to-linear bundle of 19 optical fibers (each fiber is 2-m long and has a 100-µm core diameter) with a couple of converging lenses (respectively 25 and 5 cm of focal length). The optical axis of the detection line is at a ~30° angle from the vertical incident laser. Radiation is finally introduced into a Czerny-Turner spectrometer (Kymera 328i, Andor) equipped with a 1200 l/mm grating blazed at 300 nm. An intensified CCD camera (iStar CCD 340, Andor) enables the tuning of the delay and gate parameters, as well as the gain, for signal amplification.
Our vacuum chamber is a six-way cross of 316 L in stainless steel (length 276 mm). It is equipped with a dry scroll vacuum pump (IDP-7, Agilent) and a Pirani/capacitance diaphragm gauge (PCG-750, Agilent). We use a Martian simulant gas provided by Air Liquide and composed of CO_2, with traces of Ar (1.6%) and N_2 (2.7 %). For the sake of simplicity, we often refer to this gas as CO_2. The upper part of the chamber consists in a 101-mm diameter (4 inches) and 10-mm thickness UV fused silica window, through which the laser is focused and the resulting emission is collected. The horizontal motion of the sample inside the chamber is achieved by a couple of vacuum-compatible, piezo linear stages, with a 27 mm travel (AG-LS25-27V6, Agilis) connected to a dedicated driver (AG-UC2, Agilis) controlled via a homemade LabVIEW virtual instrument (VI).

To investigate the influence of pressure of the surrounding gas on the LIBS and PIL spectral features, we started with air, and acquired a series of spectra at 0.07, 0.7, 7, 25, 70, 120, 200, 300, 400, 550, 750 mbar and 1 bar. LIBS and PIL spectra were acquired as either time-integrated spectra or time series as defined below. For time-integrated spectra, we use relatively short delay values, and large acquisition gates to detect as many photons as possible, from the feature of interest, as it decays after the laser pulse (typically $D{\sim}200\ ns$ and $G{\sim}100\ \mu s$ for atomic emissions, for example). On the other hand, for time series, we use short acquisition gates and increasing delay values, to observe the evolution of emission with time, after the laser pulse (for example D varying between $10\ ns$ and ${\sim}100\ \mu s$ and a gate $G{\sim}10\ ns$ to observe the decay of atomic emissions). We use time series to extract decay curves for different features. For both kinds of observations, the specific time parameters are tuned to the kind of emission we want to observe (e.g. shorter delays and gates for atomic emission lines than for molecular bands). To mitigate possible experimental biases and fluctuations – due for example to laser and instrument temperature variations or degassing within the chamber – we repeated our measurements as follows. For time-integrated measurements, we acquired spectra over two successive series, varying the pressure value: first decreasing it from 1 bar to 0.07 mbar, then increasing the pressure back up to 1 bar. For each given value of the pressure, we moved the target 0.5 mm to use a pristine surface for ablation and acquired five spectra at the same location, each resulting from the average of a burst of 100 laser shots. Considering that the first spectrum is often significantly different from the others – due to surface contamination or specific ablation effects at the beginning of the formation of an ablation crater – we kept only the last four spectra per point. Due to the limited size of our sample, we could not acquire multiple time series for all pressure values, and each time series is acquired on a single ablation spot.
To switch from air to Mars simulant gas, we first pumped the chamber down to a pressure of about 0.02 mbar, before injecting 7 mbar of Mars simulant gas.

The size of the plasma at maximum expansion changes from a few millimeters at 1 bar to ~5-10 mm with reduced pressures [18,38]. Therefore, there is a risk that the plasma might grow out of the field-of-view of the fiber bundle in certain experimental conditions. However, considering that our results are consistent with previous studies, as shown in section 3.1, we are confident that our field-of-view samples a representative enough portion of the plasma.

2.2. Samples

Two samples with complementary characteristics were used in this study.

The first one is a 6x6x12 mm commercial synthesized sapphire crystal (Al_2O_3) doped with titanium, similar to the crystals used as a gain medium for laser sources, and hereafter referred to as TiSa. We used this sample to investigate the evolution of plasma and PIL emissions when changing the atmospheric conditions. This sample is indeed sufficiently hard to sustain hundreds of laser shots at a given location without enduring major ablation-related damages; as a consequence, the plasma remains stable over hundreds of shots, facilitating the analyses.
The titanium is present in the crystalline matrix as Ti^{3+} and Ti^{4+}, both of which have well characterized relatively short-lived luminescence signatures [39], respectively around 400 nm and 700 nm, which are analyzed in section 3.3. Additionally, the TiSa sample contains traces of Cr^{3+}, which is

characterized by a millisecond-decay emission doublet around 693 nm, and which is used for most of this study.
As a consequence, the emission spectrum of the plasma derived from the ablation of the TiSa crystal contains different spectral features of interest, namely atomic lines (Al in particular), molecular bands (AlO); additionally, PIL signatures can be observed within the sample after ablation. We were able to choose specific features with minimal spectral overlap with each other, enabling independent observations of each.

The second sample we use is a natural Durango apatite ($Ca_5(PO_4)_3(Cl,F,OH)$) containing traces of rare-earth elements such as Sm^{3+}, Dy^{3+}, Eu^{3+}. Apatite is of particular interest in geology, because of its ability to host a wide variety of trace elements in its crystalline structure, and thus to record the ancient environmental conditions the crystal has undergone. For example, the presence of hydrogen has been exploited to study the origin of planetary water [40] and rare-earth elements contribute to trace genetic processes [9]. Moreover, apatite has previously been detected on Mars [30,32,40], in part thanks to the detection of CaF and/or CaCl emissions with LIBS. The study of this sample is therefore relevant in the context of Martian investigation, and M. Gaft et al. used a similar sample in [9] to illustrate the interest of combining LIBS and PIL observations, using time resolution, in terrestrial conditions.
Compared to TiSa, apatite is much more fragile to laser ablation, resulting in a deeper ablation crater after a series of several laser shots, and finally leading to unstable plasma emission and, possibly, sample fracturing. Moreover, Table 1 shows that several molecular bands and luminescence features overlap in the case of apatite, making the interpretation of a LIBS-PIL spectrum much more challenging. Spectra acquired on the Durango apatite crystal are presented in section 3.3.

	identification	spectral range
Molecular emission [33,34,41]	CaO	593 – 630 nm
	CaF	590 – 606 nm
	CaCl	611 – 622.5 nm
PIL features [42,43]	Sm^{3+}	Most intense signature around 598 nm; other peaks around 565 and 645 nm
	Eu^{3+}	575 and 618 nm
	Dy^{3+}	480 and 570 nm

Table 1 – Examples of molecular bands and PIL features expected to be observed by LIBS-PIL in apatite

2.3. Processing of the LIBS-PIL spectra

The experimental LIBS-PIL spectra are characterized by a continuum, atomic lines, molecular bands, from the ablation plasma, and finally PIL features emitted within the sample. The aim of this section is to describe how the spectral features were selected and the numerical data extracted to finally become the indicators of each type of spectroscopic feature.
For all spectra we first either subtract the dark spectrum or subtract the minimal value reached over the entire spectrum when no dark spectrum was recorded. Note that, because of the amplitude of noise, subtracting the minimal intensity value of the spectra results in the spectral baseline typically being around a few hundred counts.

For the TiSa sample, LIBS spectra are examined in the 298-340 nm spectral range. In this range, one can observe both a continuum and some atomic lines. The continuum signal is fitted with a third degree polynomial function over three spectral intervals: 298.0 to 304.0 nm, 311.5 to 312.0 nm, and 317.5 to 321.0 nm, in order to exclude the atomic emission lines from the calculation. Then the median of the values retrieved from the fitted function is used to track continuum intensity. The Al I atomic emission line at 309.27 nm was selected to represent atomic emission. To extract the peak intensity, we first subtract the fitted function related to the continuum to the spectrum, in the range 308.75-310.00 nm and then pick the maximum value of the continuum-corrected spectrum in the same spectral range. The corresponding spectral ranges and features are illustrated in Figure S1 in the supplementary materials. Note that if there is no signal detected from Aluminum, the resulting value corresponds to the maximal amplitude of the noise over this spectral range.
A molecular emission band related to AlO is detected between 490.0 and 530.0 nm. The (1,2) band head of the Δv = -1 sequence of the AlO $B^2\Sigma^+ - X^2\Sigma^+$ band system was selected to get the AlO signal (Figure S2). Practically, we extract the min and max intensity values in the spectral range 509.8-510.4 nm and use the difference between these two values as the AlO intensity. Based on this method, there is no need to calculate the contribution of continuum in this case. If no signal from AlO is detected, the resulting value corresponds to the amplitude of the noise over this spectral range.
Finally, regarding PIL, we use the second peak of the Cr^{3+} doublet around 693 nm. Similar to the calculation of the Al I signal, we start by fitting the continuum over the spectral intervals ranging from 680.0 to 690.0 nm, and 700.0 to 708.0 nm with a third degree polynomial function in order to exclude the Cr^{3+} doublet. Then, in the interval 693.7-695.0 nm, we subtract the fitted continuum function to the spectrum and extract the max value on the continuum-corrected signal. This value is used as the Cr^{3+} peak intensity. Note that we decided to exploit only one of the two emission lines of the doublet in order to simplify data processing.
We work under the assumption that the specific emission features that we selected are good proxies for continuum, atomic, molecular, and PIL emissions in general.

We do not extract specific emission intensities from the spectra acquired with the Durango apatite sample, but directly comment the spectra (section 3.3).

3. Results & Discussion

3.1. Influence of pressure on time-integrated PIL in air

In order to assess the feasibility of PIL on Mars, we first investigate the influence of pressure, starting with a plasma expanding in air. We thus start by examining the time-integrated LIBS and PIL spectra (Figure 1) for plasma expanding in air at 1 bar (blue) and 7 mbar (orange) after laser ablation of the TiSa sample.
Figure 1A shows both plasma continuum and Al atomic emission lines at 308.22 and 309.27 nm. In this case, the detection parameters were set to $D = 0$ and $G = 500\ \mu s$ to maximize the detection of signal related to the atomic lines. The two spectra reveal that the atomic signal-to-background ratio is significantly higher at 7 mbar than 1 bar. Moreover, some atomic emission features are clearly visible at 7 mbar, whereas they are not resolved at 1 bar, because of the overlapping continuum and spectral broadening.
Figure 1B shows the AlO molecular bands obtained for $D = 1\ \mu s$ and $G = 1\ ms$. The reduced AlO emission under 7 mbar of air compared to 1 bar is probably related to the reduced confinement of

the plasma, which results in lower probability of species interaction than in a more confined, denser plasma. Additionally, it is possible that some atmospheric oxygen may be involved in the AlO recombination at 1 bar. In this case, the reduced oxygen density at lower pressure may also contribute to reducing AlO emission under 7 mbar compared to 1 bar. However, the TiSa sample is a matrix of Al_2O_3 and the atoms of oxygen coming from the sample itself must be considered as well. Complementary tests performed under 7 mbar of argon (not shown here) showed that some AlO emission is also observed when oxygen is not present in the ambient gas, indicating that the oxygen present in the TiSa crystal contributes to molecular recombination. From these results, we can only conclude that a combination of i) the reduced reactants interaction in the larger plasma and ii) the reduced oxygen concentration at lower pressure caused the reduced AlO emission in 7 mbar compared to 1 bar. To assess the relative contributions of these two factors, further tests would be required.

Figure 1C shows the PIL signal related to Cr^{3+} in the TiSa sample, recorded for $D = 10\ \mu s$ and $G = 10\ ms$. We observe that the Cr^{3+} PIL feature is less intense at 7 mbar than 1 bar. Considering that PIL is excited by plasma emission, which is overall less intense at lower pressure, it is not surprising to observe that PIL emission is lower at 7 mbar.

The time parameters were chosen to filter out all the spectral features related to the plasma and show the PIL emission alone, based on plasma emission decay at 1 bar. However, it is interesting to notice that several atomic features – expectedly related to Al, O, Ti, Cr, or N – are visible in the spectrum acquired at 7 mbar. The strong emission line at approximately 690.32 nm can be assigned to either Cr I wide line, or the Ti I line at 690.56 nm [44]. Then, the spectral feature detected between the two Cr^{3+} lines is attributed to the Cr I wide lines at 693.40 and 693.56 nm. The other lines may be assigned to Ti I (699.75 – 700.46 – 703.33 nm) and O I (701.73, 702.55 nm). The fact that atomic emission lines are detected after 10 μs when the plasma expands in 7 mbar air is consistent with the known slower temporal decay of atomic emissions at reduced pressure [20,21]. This shows that the temporal parameters should be specifically tuned for PIL observation under Martian atmospheric pressure, in order to efficiently filter out plasma emission. To identify appropriate parameters, section 3.3 presents a comprehensive time-resolved analysis of LIBS and PIL spectra in different atmospheric conditions.

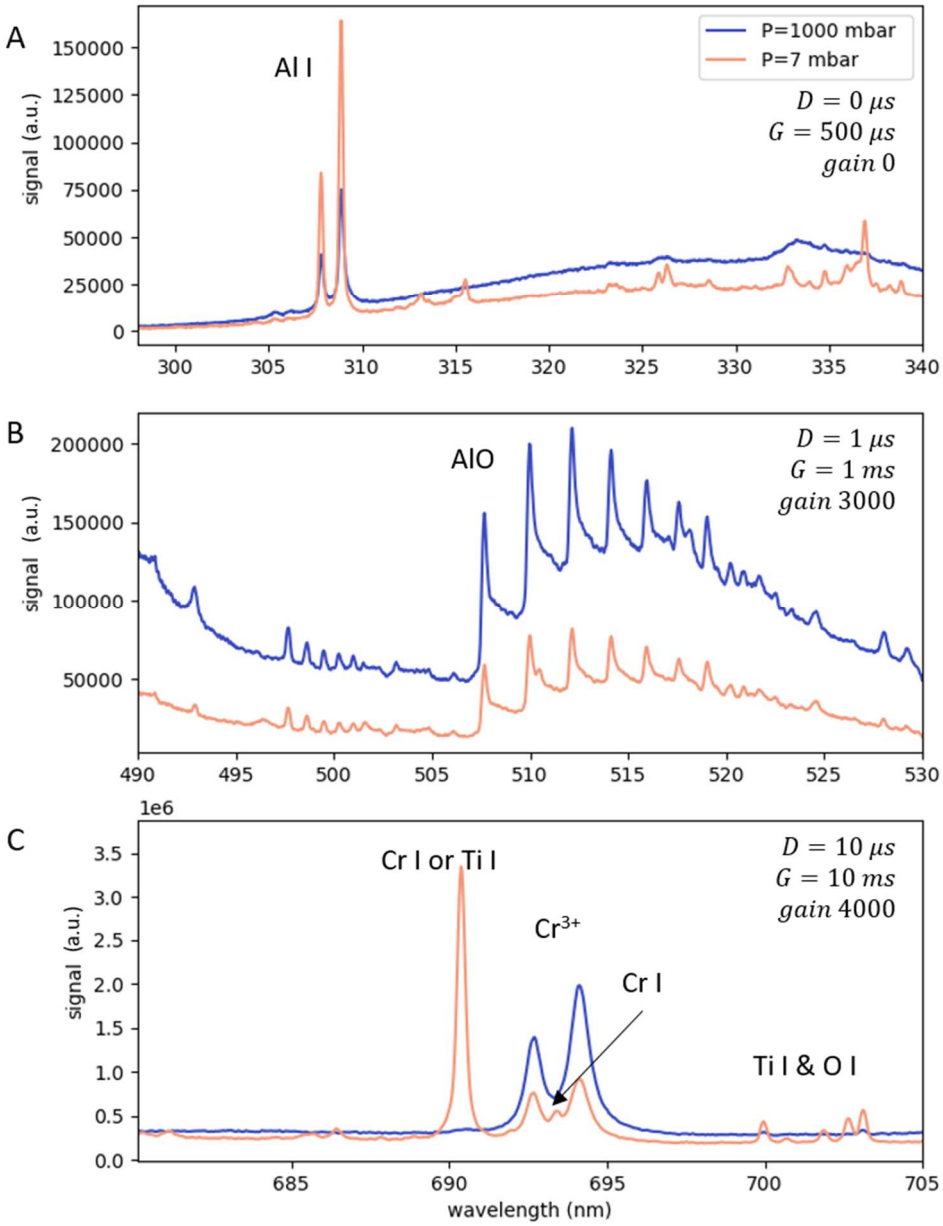

Figure 1 – LIBS & PIL spectra in selected spectral ranges after laser ablation of a TiSa crystal in 1 bar (blue) and 7 mbar (orange) of air. Each of the spectra shown here is the average of eight spectra acquired on two ablation spots in the considered conditions, each resulting from the accumulation of 100 laser shots. (A) Continuum and Al I lines at 308.22 and 309.27 nm; (B) AlO molecular bands; (C) luminescence of Cr^{3+}.

In the rest of this section, we broaden our analysis of the influence of pressure on LIBS and PIL and examine not only the pressure values corresponding to Earth and Mars atmospheric conditions, but a total of twelve values of pressure covering the range 0.07 mbar to 1 bar. The experimental parameters are the same as those used in Figure 1 and the results obtained for the twelve values of pressure are displayed in Figure 2. Figure 2Ai shows the signal of background and Figure 2Aii the signal of Al I. Then Figure 2B shows the signal of AlO and Figure 2C the signal of PIL. Note that the labels A, B, C in Figures 1 and 2 correspond to similar detection parameters. Some of the corresponding spectra are shown in Figures S3-5.

As a first result, it is interesting to notice that PIL is detected over the whole range of pressure values, despite the low-emissivity plasma obtained at 0.07 mbar (spectra shown in Figure S5).

Knight et al. published similar trends as those displayed in Figure 2Ai and 2Aii [18]. Interestingly, they demonstrated that the measured emission signal as a function of the surrounding gas pressure was not affected by the geometry of their optical setup. In the present study, we obtain very similar evolution of the continuum and atomic line with the pressure as they did, and we thus conclude that geometrical effects do not significantly affect our observations either.

Additionally, we observe that both continuum and PIL emissions are maximal around 550 mbar, whereas atomic emissions peak around 70-120 mbar and AlO is highest between 400 and 750 mbar. In the case of AlO (Figure 2B), the best condition of pressure could probably be refined by averaging over a larger number of spectra to reduce the fluctuations that we observed with our eight observations per pressure value.

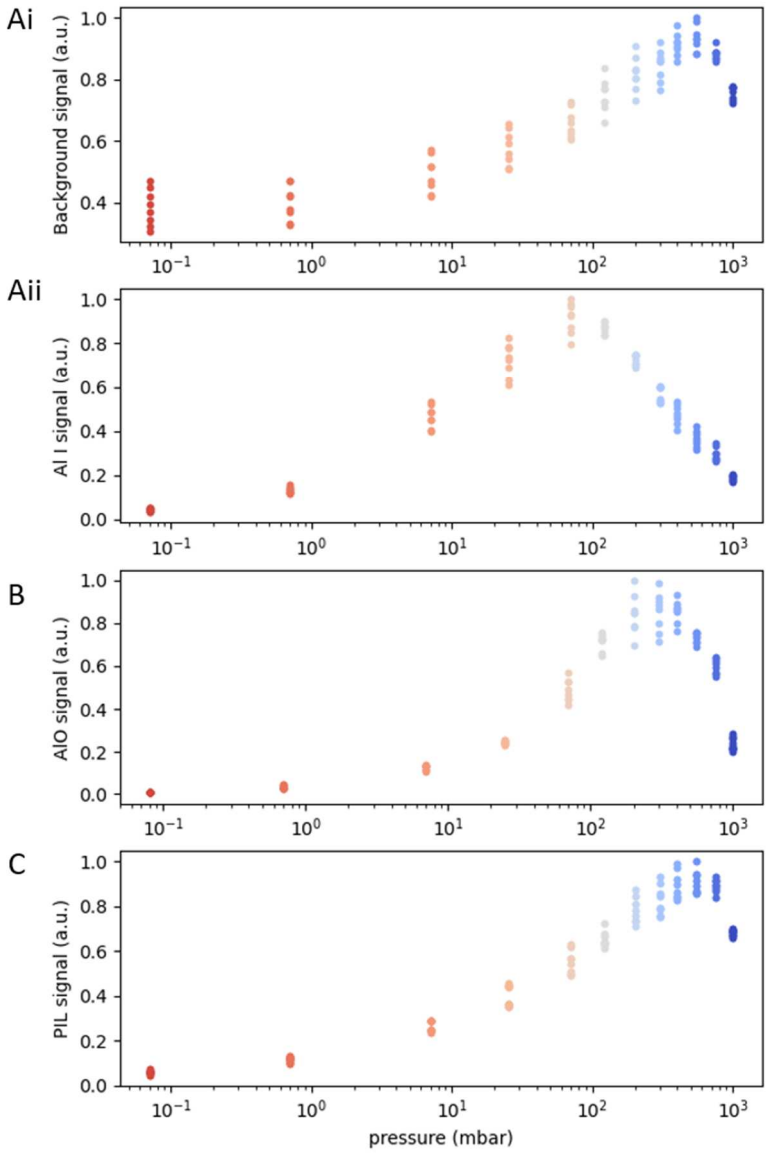

Figure 2 – Influence of the air pressure on the different signals extracted from the LIBS and PIL spectra acquired on the TiSa sample; eight spectra were acquired per pressure value, on two different ablation points. The values of pressure are given on a logarithmic scale (in mbar). Features intensity were extracted as described in section 2.3 and normalized to unity; (Ai) continuum; (Aii) Al I line at 309.27 nm (B) AlO molecular band at 510 nm; (C) plasma-induced luminescence of Cr^{3+} at 693-694 nm.

To conclude this study on pressure influence on time-integrated PIL, we investigate the presence of correlations between PIL and plasma emissions, to better understand the excitation source of PIL. Figure 3A shows a very good correlation between the PIL and the continuum signals. Moreover, it was previously shown that PIL excitation under 1 bar of air is dominated by plasma continuum emission [10]. From the combination of these two observations, we conclude that continuum emission plays a significant role in PIL excitation over the whole range of pressure examined here, namely 0.07 mbar to 1 bar. Looking at the comparison of PIL signal with atomic and molecular emission signals (Figures 3B-C), we observe no such significant correlation as with continuum emission over the whole range of pressure values investigated here. This possibly confirms the significance of continuum emission contribution to PIL excitation. However, it is also possible that other atomic and molecular features – maybe in the UV region – may be more correlated to PIL emissions than those considered here; in that case, we would not see the contribution of these features by looking only at the 308 nm Al I line and the 510 nm AlO band head.
The balance between continuum, atomic and molecular emission signatures in the PIL excitation process could be further investigated by looking at more features, and/or using the *side PIL* configuration with different ablation targets [10].

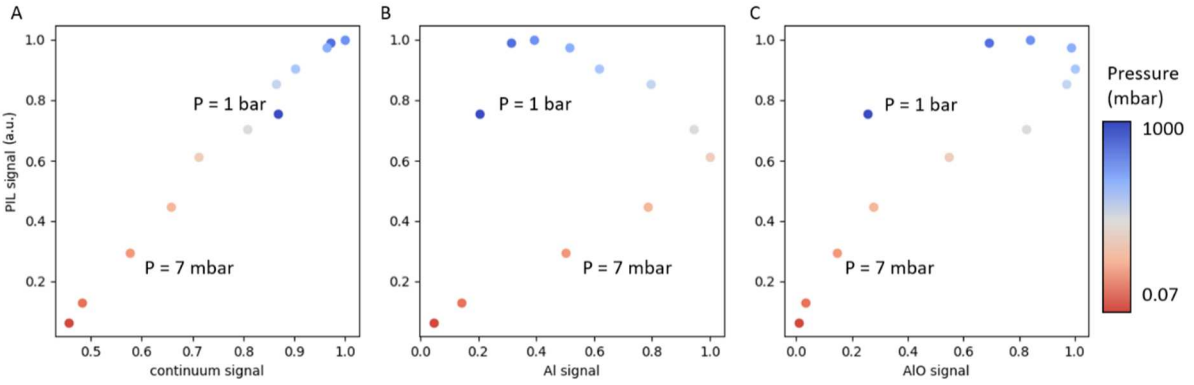

Figure 3 – Comparison of PIL and plasma emissions (A) continuum, (B) Al I atomic emission line (C) AlO molecular band, each normalized to its maximum value. Emission intensities obtained at 0.07, 0.7, 7, 25, 70, 120, 200, 300, 400, 550, 750 mbar and 1 bar on our TiSa sample; colors corresponding to pressure values, like in Figure 2. The intensity values plotted here correspond to the average values of the eight observations per pressure values displayed in Figure 2.

To summarize, we showed that: i) PIL emissions, in air, are detected at all pressure values tested between 0.07 mbar and 1 bar; ii) PIL emissions are most intense under 550 mbar of air; iii) the variation of PIL with pressure are related to changes in continuum emission from the laser-induced plasma. As a reminder, reduced continuum emission at lower pressure is due to the reduced plasma confinement, which favors faster plasma expansion, and therefore rapidly decreasing temperature and density.

3.2. Influence of the ambient gas – air/Mars simulant comparison

In this section, we investigate the effect of changing the gas in which the plasma expands from air to CO_2. The time parameters are the same as in the previous sections, except for the PIL detection. Indeed, previous PIL observations under 7 mbar of air showed that atomic emissions are still significant after a delay of 10 μs in such pressure conditions (Figure 1C). To filter out these emissions, in the following section, we observe PIL emission with a delay $D = 200\ \mu s$. Such a long delay is still very satisfying when we analyze long-lived PIL features.

Figure 4 shows the LIBS (4A-B) and PIL (4C) spectra obtained at 7 mbar when the laser induced plasma expands in air (blue) and CO_2 (red). As far as we're aware, the red spectrum presented in Figure 4C is the first PIL spectrum in Martian-like atmospheric conditions published so far. Figure 4C clearly shows that PIL does not change when changing the gas composition from air to CO_2. Since we established that PIL emission is correlated to plasma continuum emission, and the latter is not affected by the change in gas composition (Figure 4A), this is all consistent. Interestingly, it indicates that the results established in the previous section about the evolution of PIL intensity with atmospheric pressure in air can probably be generalized to CO_2.

Moreover, if the atomic emission lines are not affected by gas composition either (Figure 4A), we observe that the AlO signal is two to three times more intense in CO_2 than in air (Figure 4B). Although there is a significant variability within the set of four spectra corresponding to AlO emissions in each condition, the signal is consistently more intense in CO_2 than in air. This might be explained in part by the fact that, for a given value of pressure, the density of oxygen atoms is higher in Mars-like atmosphere than in air, increasing the probability of AlO recombination. In addition, the efficiency of energy transfers between the plasma and the ambient gas may be different in air and Mars simulant. This could result in molecular recombination being facilitated in Martian conditions compared to terrestrial ones, though this should be investigated further.

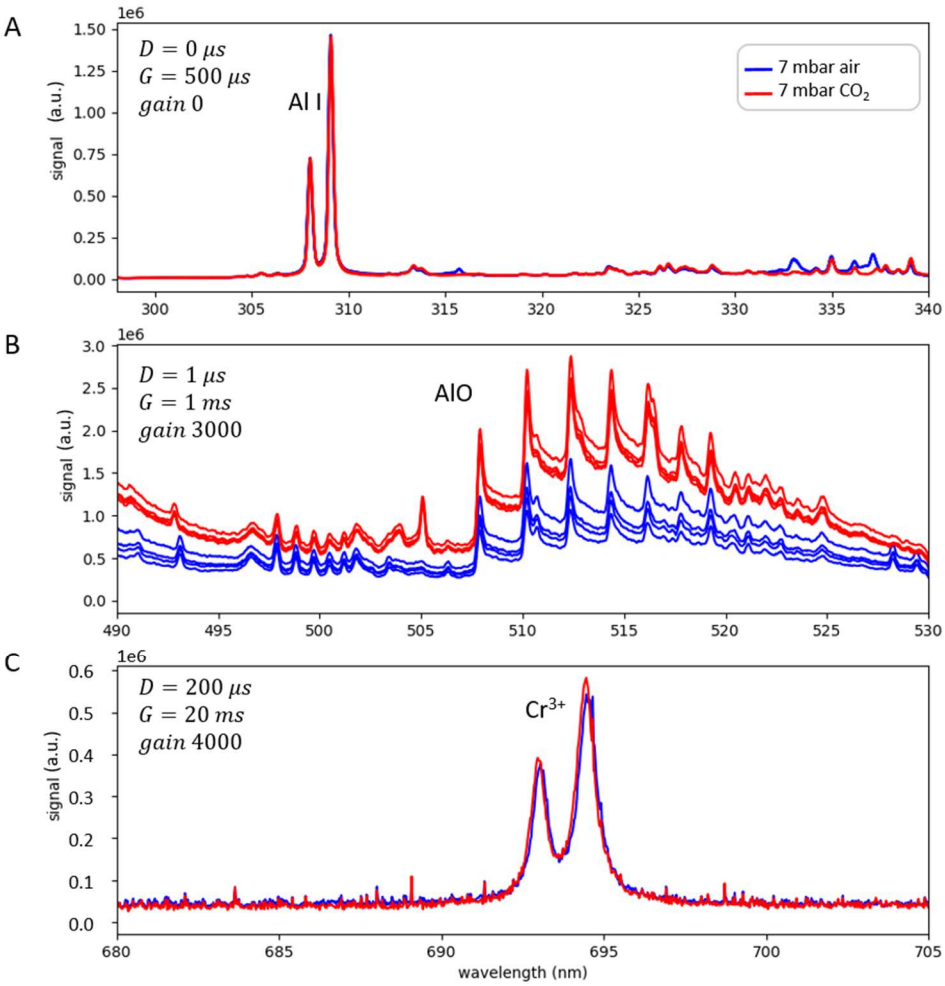

Figure 4 – LIBS and PIL spectra from ablation of a titanium doped sapphire crystal (TiSa) under 7 mbar of air (blue) and *CO_2* (red). We show four spectra per set of atmospheric conditions, acquired on the same ablation point, to monitor the repeatability of the measurements. (A) continuum and Al I emission; (B) AlO emission; (C) PIL signature of Cr^{3+}.

3.3. Temporal behavior of LIBS features and implications for PIL

We observed in section 2.3 that temporal parameters optimized for terrestrial PIL do not enable to filter out plasma emissions efficiently in Martian atmospheric conditions. In this section, we take a closer look at several plasma emission decays to find out optimal conditions that minimize overlap between PIL and LIBS features. As for the previous sections, we use the TiSa sample for detailed analyses; we then investigate how the lessons-learned can be used to acquire Martian PIL spectra on a natural sample: the Durango apatite.

Figure 5 displays the decay curves of three types of LIBS features, namely continuum (5A), Al I atomic emission line (5B), and AlO molecular emission band (5C), monitored in the case of TiSa sample. These decay curves are presented for plasma expansion in 1 bar of air (blue), 7 mbar of air (black), and 7 mbar of CO_2 (red).

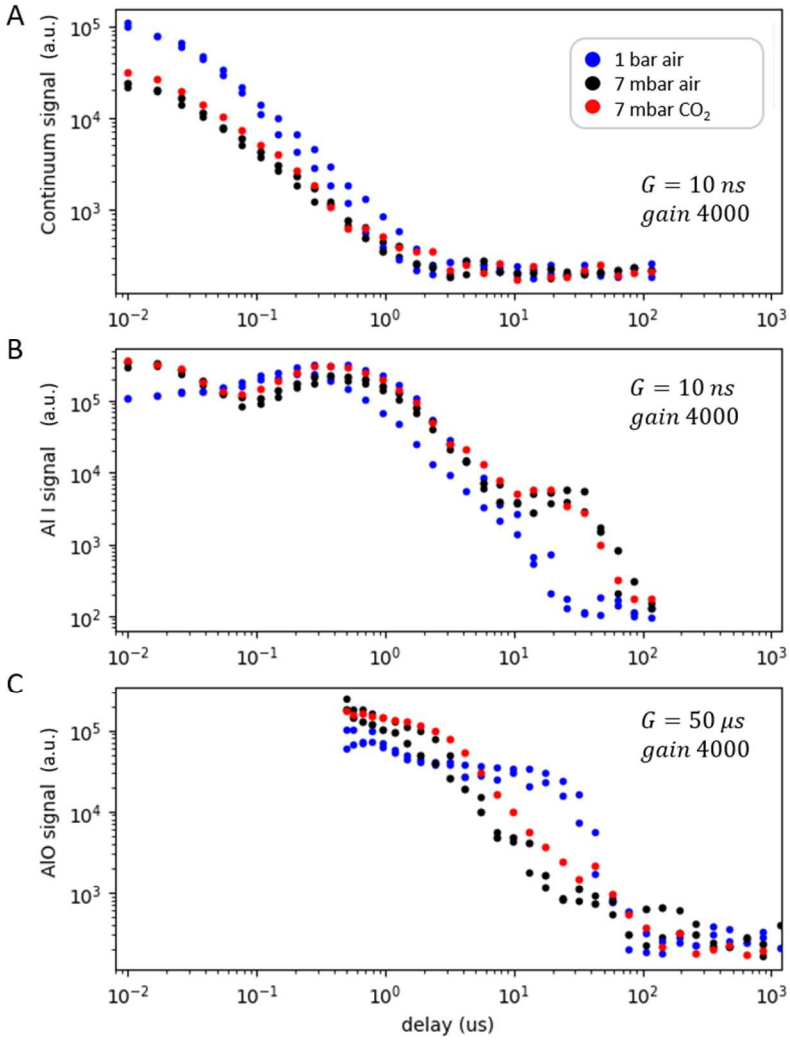

Figure 5 – Plasma emission decay curves, from the ablation of TiSa in 1 bar of air (blue), 7 mbar of air (black) and 7 mbar of CO_2 (red). (A) continuum (B) Al I signal (C) molecular emission.

We see from Figure 5 that changing the pressure of air from 1 bar to 7 mbar affects the temporal behaviors of the three types of emissions much more than changing – at 7 mbar – the gas from air to CO_2. This is consistent with the conclusion drawn from the time-integrated spectra in sections 3.1 and 3.2. In addition, the decay curves of Al I related to 7 mbar, in both air and CO_2, exhibit a plateau

between ~8 and ~50 μs (Figure 5B) resulting in overall longer-lived atomic emissions at reduced pressure, which is consistent with the conclusions of previous studies [20]. Regarding the AlO molecular emission signal (Figure 5C), we observe again a clear difference between the decay curve corresponding to 1 bar which shows a plateau and the ones acquired at 7 mbar which decrease continuously. Depending on the temporal range considered, Figure 5C reveals that molecular emissions can be higher in either terrestrial or Martian conditions.

Overall, whether it is atomic or molecular emissions, in the different atmospheric conditions investigated here, plasma emissions remain significant until about 80-100 μs after the laser pulse. We can therefore anticipate that the detection of short-lived PIL features (typically up to tens of microseconds) will be challenging under Martian condition, like in terrestrial conditions [34], especially for signatures that may spectrally overlap with other spectral features related to plasma emissions.

This assertion is easily verified through the PIL detection of the Ti^{3+} and Ti^{4+} ions present in the TiSa sample. Their corresponding spectral features have already been presented for experimental conditions corresponding to PIL in air under 1 bar pressure [10], though with some overlapping atomic signatures in the case of Ti^{3+}. It is interesting to note that, so far, we failed to observe either of these signature with PIL in Mars-like atmospheric conditions. Regarding Ti^{3+}, it's fairly easy to understand, since its emission happens in the first tens of microseconds after excitation, and Figure 5B shows clearly that atomic emissions are much stronger between ~8 and 50 μs in Martian than terrestrial conditions. As a consequence, the lower-signal PIL emission is hidden by the longer-lived atomic emissions in Mars-like conditions, which, for a given gain, are still more than an order of magnitude more intense than PIL emissions at that time. For Ti^{4+}, the lack of detection is harder to understand. There is no obvious overlap with LIBS features between 380 and 440 nm for the chosen value of delay ($D = 50\ \mu s$) since AlO emission band starts around 440 nm, as evidenced in terrestrial conditions, where both Ti^{4+} and AlO emissions can be observed side-by-side for delays around $30\ \mu s$ (not shown here). A possible explanation could be that the UV photons in the spectral range 200 and 260 nm that are required to excite the Ti^{4+} ions [39] might be significantly less numerous at 7 mbar, due to the faster temperature decay, such that the PIL feature of Ti^{4+} is not detected. Regarding long-lived signatures, on the other hand, it seems that, for delay values superior or equal to 100 μs, PIL emissions in TiSa should be observable with minimal interference from plasma emissions. This explains why Cr^{3+} PIL observation was relatively easy in all of the atmospheric conditions examined in this study (Figures 1C and 4C).

To conclude, although we observe important differences in the decay curves acquired in terrestrial and simulated Martian atmosphere, the total lifetime of plasma emissions is rather similar, around 80-100 μs. As a consequence, we expect that most short-lived luminescence features will be hard to observe with Martian PIL, as already noted with terrestrial PIL. Interestingly, we've had even more difficulties to observe some short-lived emissions with Martian PIL than in terrestrial conditions. However, we've only looked at three luminescence signatures; more luminescence centers should be investigated to conclude on the relative difficulties posed by Martian and terrestrial PIL for short-lived signature observation.

Finally, the influence of the temporal characteristics of the plasma emission on the decay of the Cr^{3+} emission within the sample has been investigated by comparing Martian PIL to TRLS, that is luminescence excited by a laser beam at 532-nm, with 5-ns laser pulse duration, as used by

SuperCam. Figure 6 thus shows the decay curves corresponding to the normalized Cr^{3+} signal with both of these excitation techniques. PIL data points (red) are reported only after 1 µs because PIL and LIBS signals spatially overlap and significant decay of LIBS signal is required to get relevant PIL data. Moreover, the TRLS signal (green) is considerably more intense than the PIL one, enabling to record the Cr^{3+} emission without amplification gain, and up to higher delay values. This figure shows that the normalized PIL and TRLS decay curves overlap perfectly. It indicates that i) the LIBS signal responsible for PIL – and especially the continuum signal (1-μs decay) can be considered as sufficiently short compared to the decay of the Cr^{3+} luminescence, and ii) PIL and TRLS excitations are mainly based on the involvement of the same energy levels for the excited state. However, this last statement could be wrong in other cases – other crystals – where plasma emission could excite other upper levels than TRLS.

This observation shows that, temporal decay of PIL in Martian atmospheric conditions can be used to identify the luminescence center involved in the spectral feature, as often down in luminescence spectroscopy.

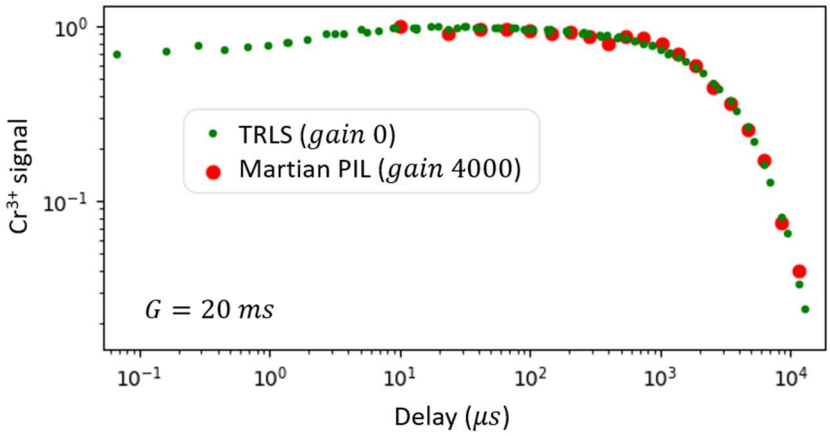

Figure 6 – Decay of Cr^{3+} emission, excited in Martian PIL (red) and TRLS (green) configurations. We use the same gate $G = 20\ ms$, but different gains. The curves are normalized to the maximal Cr^{3+} emission intensity.

We extend our study to the natural Durango apatite sample, to see whether some trivalent rare-earth ions, which are not detected with LIBS, can be observed with Martian PIL. The signatures of Sm^{3+}, Eu^{3+} and Dy^{3+}, which are present in the sample, are described in Table 1, as are the molecular features that may overlap with the luminescence emission bands.

We first tried acquiring a Martian PIL spectrum with a delay $D = 100\ \mu s$ and a gate of $20\ ms$, because of the decay observations performed on TiSa, and the subsequent conclusion that most plasma emissions were gone after around 100 μs. However, the resulting spectrum (not shown here) was difficult to interpret, due to features overlap. To unmix the signatures, we observe the evolution of the signal between $D = 50\ \mu s$ and $D = 23.3\ ms$, as shown in Figure 7A-B. From these series, we can identify two different features: a broad band centered around 605 nm, which decays continuously between 50 and $\sim 200\ \mu s$; and a sharper signature, centered at 598 nm, with lower intensity for $D < 200\ \mu s$ and slower decay. The decay rates indicate that the former is probably a molecular feature – though it is hard to discriminate between CaF and CaO – whereas the latter must be a millisecond-decay PIL signature and matches the Sm^{3+} band. From the time series, we can thus choose specific time windows to observe the two signatures separately; the corresponding spectra are shown in Figure 7C-D. From Figure 7C, we can definitely identify the molecular band as CaF. In Figure 7D, we observe not only the 598 nm band of Sm^{3+}, but also the 550 and 650 nm bands of Sm^{3+},

the presence of which reinforce the identification of the first band. The 480 and 580 nm bands could be due to either Dy^{3+},or Tb^{3+}; although the latter could also explain the small bands visible between 400 and 450 nm [45,46]. Interestingly, Eu^{3+} (575 and 618 nm) was not detected with Martian PIL, whereas it can be clearly detected with time-resolved luminescence spectroscopy, based on pulsed laser excitation at 532 nm (see Figure S6). However, it should be noticed that this spectral feature was not detected either in the frame of *remote PIL* in 1 bar of air [10]. By consequence, the absence of this spectral feature is not related to the Mars-like atmospheric conditions but rather to more general PIL excitation. Overall, we can note that the broad excitation range involved in PIL can excite simultaneously many luminescence centers present in the crystal, resulting in complex luminescence spectra, with overlapping and possibly broadened bands.

Finally, since we observed from Figure 5 that plasma emissions are mostly gone after $100\ \mu s$, one might be surprised to find such significant overlap of molecular and PIL emissions between 100 and $200\ \mu s$ as shown in Figure 7A. The explanation is two-fold. First, the $100\ \mu s$ time frame was identified for another sample, the TiSa crystal, with different hardness, composition and molecular emissions than those of the Durango apatite. The plasma temperature as well as density of the reactants are therefore different and may result in slightly different decays of molecular species. Moreover, the overall intensity of molecular emission is significantly more intense than that of PIL. As a consequence, the remaining molecular signal that may be considered very small compared to the maximum molecular emission, may still be significant compared to PIL emission.

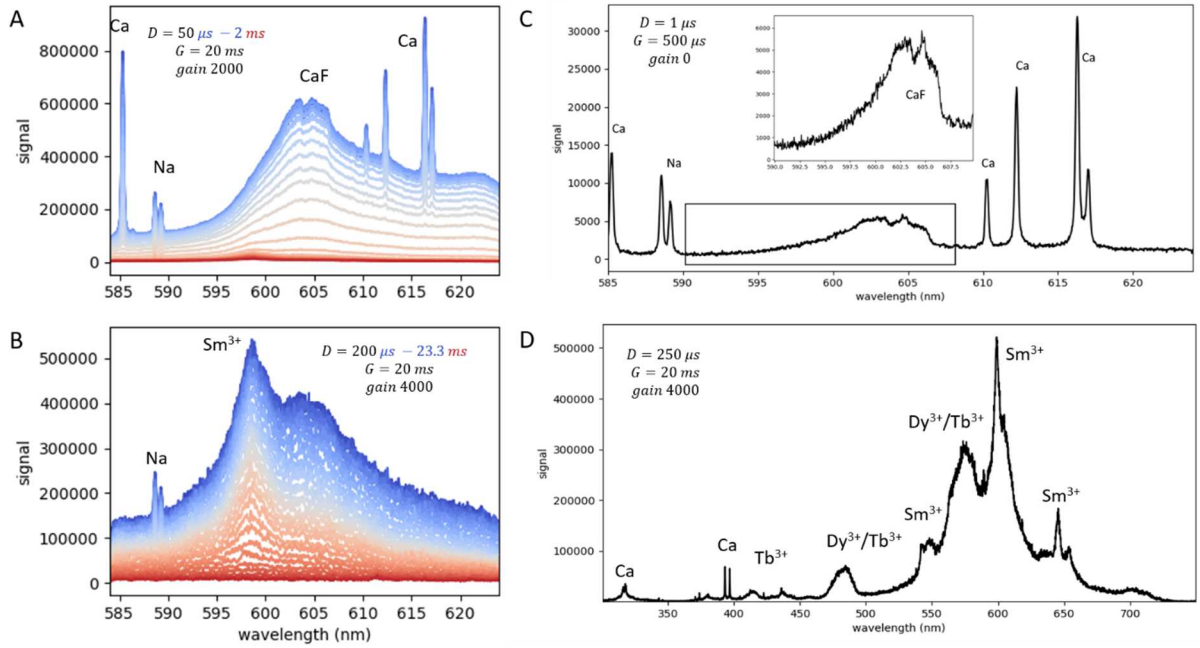

Figure 7 – Looking for PIL emission of trivalent rare-earth elements in our Durango apatite sample. (A-B) time series showing the decay of plasma then PIL emissions in the 580-625 nm range. (C) Observation of the molecular signature, with time parameters derived from the time series. (D) PIL spectrum (accumulation of 50 laser shots). (C-D) Assemblages of spectra acquired over different 40-nm wide spectral ranges to cover these large spectral windows.

4. Conclusion & perspectives

The SuperCam instrument provides the first opportunity to perform LIBS as well as time-resolved spectroscopy on Mars, and therefore to observe plasma-induced luminescence (PIL) within the

analyzed sample, after most plasma emission has decayed. In the present study, we acquire the first PIL spectra in Mars-like atmospheric conditions, to our knowledge, and thus show that PIL can be potentially performed by SuperCam on Mars. We have successfully run parametric studies on a synthetized titanium doped sapphire crystal and demonstrated that PIL can be applied to analyze natural samples through the use of a Durango apatite crystal. We demonstrated that PIL signal is very well correlated with the continuum signal of the LIBS spectrum for pressure values between 0.07 mbar and 1 bar, and that PIL emission is much more affected by the gas pressure than by changing the gas from air to Mars simulant. From a comparison of the time decays of continuum, atomic lines and molecular bands in various atmospheric conditions, we conclude that, just like in terrestrial conditions, it is extremely challenging to use Martian PIL to observe short-decay PIL features. Moreover, relatively long delay ($\geq 200\ \mu s$ with our experimental conditions) was necessary to filter out most of plasma emissions in Mars-like conditions, especially to separate the CaF molecular signal from the Sm^{3+} PIL feature in the Durango apatite.

This study is therefore a first step towards understanding if and how PIL spectroscopy could complement the techniques made available by SuperCam on Mars, and used to characterize Martian soil and rocks along the traverse of the Perseverance rover.

Future studies could investigate the performance of Martian PIL for the analysis of geologic samples, composed of either monophasic or multiphasic microcrystals, as opposed to the macro crystals used in this study. Moreover, the respective advantages of time-resolved luminescence spectroscopy (TRLS) using an excitation wavelength of 532 nm – as currently implemented with SuperCam – and Martian PIL should be compared. Indeed, the broad range of plasma emissions, used as PIL excitation, can excite, and thus reveal, luminescence centers that are not excited at 532 nm. However, this also results in a more significant overlap of luminescence signatures. Together with the low sensitivity of the signals, this is one of the major challenges for the application of PIL on Mars. Another important point to consider is that PIL ablates and damages the sample surface, while TRLS is destruction-free. TRLS therefore has the advantage that a measurement can be improved by increasing the number of laser shots on the sample, while this is not possible with PIL without changing the investigated sample surface. This currently limits the applicability of PIL on Mars, since some of the most relevant samples to investigate with PIL include small, fragile crystals that cannot be measured multiple times. Future studies on PIL for the application on Mars should therefore focus on methods to improve the sensitivity of the technique without requiring additional laser shots. This could be achieved by further optimization of the detector settings such as delay, gate, and gain, which have been shown in this study to have a large influence on the detected signals.

Funding

This work was supported by CNES and Region Nouvelle Aquitaine.

Acknowledgements:

Our thanks to Nikita Fedorov (CELIA – Université de Bordeaux, CNRS, CEA) for helping us with the design and setup of the climatic chamber and to Arnaud Sauveur-Sanchez (CELIA – Université de Bordeaux, CNRS, CEA) for the linear stages automatization VI.

References

[1] S. Maurice, R.C. Wiens, P. Bernardi, P. Caïs, S. Robinson, T. Nelson, O. Gasnault, J.-M. Reess, M. Deleuze, F. Rull, J.-A. Manrique, S. Abbaki, R.B. Anderson, Y. André, S.M. Angel, G. Arana, T. Battault, P. Beck, K. Benzerara, S. Bernard, J.-P. Berthias, O. Beyssac, M. Bonafous, B. Bousquet, M. Boutillier, A. Cadu, K. Castro, F. Chapron, B. Chide, K. Clark, E. Clavé, S. Clegg, E. Cloutis, C. Collin, E.C. Cordoba, A. Cousin, J.-C. Dameury, W. D'Anna, Y. Daydou, A. Debus, L. Deflores, E. Dehouck, D. Delapp, G. De Los Santos, C. Donny, A. Doressoundiram, G. Dromart, B. Dubois, A. Dufour, M. Dupieux, M. Egan, J. Ervin, C. Fabre, A. Fau, W. Fischer, O. Forni, T. Fouchet, J. Frydenvang, S. Gauffre, M. Gauthier, V. Gharakanian, O. Gilard, I. Gontijo, R. Gonzalez, D. Granena, J. Grotzinger, R. Hassen-Khodja, M. Heim, Y. Hello, G. Hervet, O. Humeau, X. Jacob, S. Jacquinod, J.R. Johnson, D. Kouach, G. Lacombe, N. Lanza, L. Lapauw, J. Laserna, J. Lasue, L. Le Deit, S. Le Mouélic, E. Le Comte, Q.-M. Lee, C. Legett, R. Leveille, E. Lewin, C. Leyrat, G. Lopez-Reyes, R. Lorenz, B. Lucero, J.M. Madariaga, S. Madsen, M. Madsen, N. Mangold, F. Manni, J.-F. Mariscal, J. Martinez-Frias, K. Mathieu, R. Mathon, K.P. McCabe, T. McConnochie, S.M. McLennan, J. Mekki, N. Melikechi, P.-Y. Meslin, Y. Micheau, Y. Michel, J.M. Michel, D. Mimoun, A. Misra, G. Montagnac, C. Montaron, F. Montmessin, J. Moros, V. Mousset, Y. Morizet, N. Murdoch, R.T. Newell, H. Newsom, N. Nguyen Tuong, A.M. Ollila, G. Orttner, L. Oudda, L. Pares, J. Parisot, Y. Parot, R. Pérez, D. Pheav, L. Picot, P. Pilleri, C. Pilorget, P. Pinet, G. Pont, F. Poulet, C. Quantin-Nataf, B. Quertier, D. Rambaud, W. Rapin, P. Romano, L. Roucayrol, C. Royer, M. Ruellan, B.F. Sandoval, V. Sautter, M.J. Schoppers, S. Schröder, H.-C. Seran, S.K. Sharma, P. Sobron, M. Sodki, A. Sournac, V. Sridhar, D. Standarovsky, S. Storms, N. Striebig, M. Tatat, M. Toplis, I. Torre-Fdez, N. Toulemont, C. Velasco, M. Veneranda, D. Venhaus, C. Virmontois, M. Viso, P. Willis, K.W. Wong, The SuperCam Instrument Suite on the Mars 2020 Rover: Science Objectives and Mast-Unit Description, Space Sci Rev. 217 (2021) 47. https://doi.org/10.1007/s11214-021-00807-w.

[2] R.C. Wiens, S. Maurice, S.H. Robinson, A.E. Nelson, P. Cais, P. Bernardi, R.T. Newell, S. Clegg, S.K. Sharma, S. Storms, J. Deming, D. Beckman, A.M. Ollila, O. Gasnault, R.B. Anderson, Y. André, S. Michael Angel, G. Arana, E. Auden, P. Beck, J. Becker, K. Benzerara, S. Bernard, O. Beyssac, L. Borges, B. Bousquet, K. Boyd, M. Caffrey, J. Carlson, K. Castro, J. Celis, B. Chide, K. Clark, E. Cloutis, E.C. Cordoba, A. Cousin, M. Dale, L. Deflores, D. Delapp, M. Deleuze, M. Dirmyer, C. Donny, G. Dromart, M. George Duran, M. Egan, J. Ervin, C. Fabre, A. Fau, W. Fischer, O. Forni, T. Fouchet, R. Fresquez, J. Frydenvang, D. Gasway, I. Gontijo, J. Grotzinger, X. Jacob, S. Jacquinod, J.R. Johnson, R.A. Klisiewicz, J. Lake, N. Lanza, J. Laserna, J. Lasue, S. Le Mouélic, C. Legett, R. Leveille, E. Lewin, G. Lopez-Reyes, R. Lorenz, E. Lorigny, S.P. Love, B. Lucero, J.M. Madariaga, M. Madsen, S. Madsen, N. Mangold, J.A. Manrique, J.P. Martinez, J. Martinez-Frias, K.P. McCabe, T.H. McConnochie, J.M. McGlown, S.M. McLennan, N. Melikechi, P.-Y. Meslin, J.M. Michel, D. Mimoun, A. Misra, G. Montagnac, F. Montmessin, V. Mousset, N. Murdoch, H. Newsom, L.A. Ott, Z.R. Ousnamer, L. Pares, Y. Parot, R. Pawluczyk, C. Glen Peterson, P. Pilleri, P. Pinet, G. Pont, F. Poulet, C. Provost, B. Quertier, H. Quinn, W. Rapin, J.-M. Reess, A.H. Regan, A.L. Reyes-Newell, P.J. Romano, C. Royer, F. Rull, B. Sandoval, J.H. Sarrao, V. Sautter, M.J. Schoppers, S. Schröder, D. Seitz, T. Shepherd, P. Sobron, B. Dubois, V. Sridhar, M.J. Toplis, I. Torre-Fdez, I.A. Trettel, M. Underwood, A. Valdez, J. Valdez, D. Venhaus, P. Willis, The SuperCam Instrument Suite on the NASA Mars 2020 Rover: Body Unit and Combined System Tests, Space Sci Rev. 217 (2021) 4. https://doi.org/10.1007/s11214-020-00777-5.

[3] J.A. Manrique, G. Lopez-Reyes, A. Cousin, F. Rull, S. Maurice, R.C. Wiens, M.B. Madsen, J.M. Madariaga, O. Gasnault, J. Aramendia, G. Arana, P. Beck, S. Bernard, P. Bernardi, M.H. Bernt, A. Berrocal, O. Beyssac, P. Caïs, C. Castro, K. Castro, S.M. Clegg, E. Cloutis, G. Dromart, C. Drouet, B. Dubois, D. Escribano, C. Fabre, A. Fernandez, O. Forni, V. Garcia-Baonza, I. Gontijo, J. Johnson, J. Laserna, J. Lasue, S. Madsen, E. Mateo-Marti, J. Medina, P.-Y. Meslin, G. Montagnac, A. Moral, J. Moros, A.M. Ollila, C. Ortega, O. Prieto-Ballesteros, J.M. Reess, S. Robinson, J. Rodriguez, J. Saiz, J.A. Sanz-Arranz, I. Sard, V. Sautter, P. Sobron, M. Toplis, M. Veneranda,

SuperCam Calibration Targets: Design and Development, Space Sci Rev. 216 (2020) 138. https://doi.org/10.1007/s11214-020-00764-w.

[4] A. Cousin, V. Sautter, C. Fabre, G. Dromart, G. Montagnac, C. Drouet, P.Y. Meslin, O. Gasnault, O. Beyssac, S. Bernard, E. Cloutis, O. Forni, P. Beck, T. Fouchet, J.R. Johnson, J. Lasue, A.M. Ollila, P. De Parseval, S. Gouy, B. Caron, J.M. Madariaga, G. Arana, M.B. Madsen, J. Laserna, J. Moros, J.A. Manrique, G. Lopez-Reyes, F. Rull, S. Maurice, R.C. Wiens, SuperCam calibration targets on board the perseverance rover: Fabrication and quantitative characterization, Spectrochimica Acta Part B: Atomic Spectroscopy. 188 (2022) 106341. https://doi.org/10.1016/j.sab.2021.106341.

[5] S. Maurice, B. Chide, N. Murdoch, R.D. Lorenz, D. Mimoun, R.C. Wiens, A. Stott, X. Jacob, T. Bertrand, F. Montmessin, N.L. Lanza, C. Alvarez-Llamas, S.M. Angel, M. Aung, J. Balaram, O. Beyssac, A. Cousin, G. Delory, O. Forni, T. Fouchet, O. Gasnault, H. Grip, M. Hecht, J. Hoffman, J. Laserna, J. Lasue, J. Maki, J. McClean, P.-Y. Meslin, S. Le Mouélic, A. Munguira, C.E. Newman, J.A. Rodríguez Manfredi, J. Moros, A. Ollila, P. Pilleri, S. Schröder, M. de la Torre Juárez, T. Tzanetos, K.M. Stack, K. Farley, K. Williford, the SuperCam team, R.C. Wiens, T. Acosta-Maeda, R.B. Anderson, D.M. Applin, G. Arana, M. Bassas-Portus, R. Beal, P. Beck, K. Benzerara, S. Bernard, P. Bernardi, T. Bosak, B. Bousquet, A. Brown, A. Cadu, P. Caïs, K. Castro, E. Clavé, S.M. Clegg, E. Cloutis, S. Connell, A. Debus, E. Dehouck, D. Delapp, C. Donny, A. Dorresoundiram, G. Dromart, B. Dubois, C. Fabre, A. Fau, W. Fischer, R. Francis, J. Frydenvang, T. Gabriel, E. Gibbons, I. Gontijo, J.R. Johnson, H. Kalucha, E. Kelly, E.W. Knutsen, G. Lacombe, S. Le Mouélic, C. Legett, R. Leveille, E. Lewin, G. Lopez-Reyes, E. Lorigny, J.M. Madariaga, M. Madsen, S. Madsen, L. Mandon, N. Mangold, M. Mann, J.-A. Manrique, J. Martinez-Frias, L.E. Mayhew, T. McConnochie, S.M. McLennan, N. Melikechi, F. Meunier, G. Montagnac, V. Mousset, T. Nelson, R.T. Newell, Y. Parot, C. Pilorget, P. Pinet, G. Pont, F. Poulet, C. Quantin-Nataf, B. Quertier, W. Rapin, A. Reyes-Newell, S. Robinson, L. Rochas, C. Royer, F. Rull, V. Sautter, S. Sharma, V. Shridar, A. Sournac, M. Toplis, I. Torre-Fdez, N. Turenne, A. Udry, M. Veneranda, D. Venhaus, D. Vogt, P. Willis, In situ recording of Mars soundscape, Nature. (2022). https://doi.org/10.1038/s41586-022-04679-0.

[6] R.C. Wiens, A. Udry, N. Mangold, O. Beyssac, C. Quantin, V. Sautter, A. Cousin, A. Brown, T. Bosak, L. Mandon, O. Forni, J.R. Johnson, S. McLennan, C.L. Iv, S. Maurice, L. Mayhew, L. Crumpler, R.B. Anderson, S.M. Clegg, A.M. Ollila, J. Hall, P. Gasda, J.I. Simon, E.M. Hausrath, B. Horgan, F. Poulet, P. Beck, S. Gupta, B. Chide, S. Connell, E. Dehouck, G. Dromart, T. Fouchet, C. Royer, J. Frydenvang, O. Gasnault, H. Kalucha, N. Lanza, J. Lasue, S.L. Mouelic, R. Leveillé, E. Cloutis, G.L. Reyes, K. Castro, J.M. Madariaga, E. Kelly, F. Montmessin, W. Fischer, R. Francis, K. Stack, K. Farley, Composition and density stratification observed by SuperCam in the first 300 sols in Jezero crater, in: 2022: p. 2075.

[7] R.B. Anderson, O. Forni, A. Cousin, R.C. Wiens, S.M. Clegg, J. Frydenvang, T.S.J. Gabriel, A. Ollila, S. Schröder, O. Beyssac, E. Gibbons, D.S. Vogt, E. Clavé, J.-A. Manrique, I.V. Carey Legett, P. Pilleri, R.T. Newell, J. Sarrao, S. Maurice, G. Arana, K. Benzerara, P. Bernardi, S. Bernard, B. Bousquet, A.J. Brown, C. Alvarez-Llamas, B. Chide, E. Cloutis, J. Comellas, S. Connell, E. Dehouck, D.M. Delapp, A. Essunfeld, C. Fabre, T. Fouchet, C. Garcia-Florentino, L. García-Gómez, P. Gasda, O. Gasnault, E.M. Hausrath, N.L. Lanza, J. Laserna, J. Lasue, G. Lopez, J.M. Madariaga, L. Mandon, N. Mangold, P.-Y. Meslin, A.E. Nelson, H. Newsom, A.L. Reyes-Newell, S. Robinson, F. Rull, S. Sharma, J.I. Simon, P. Sobron, I.T. Fernandez, A. Udry, D. Venhaus, S.M. McLennan, R.V. Morris, B. Ehlmann, Post-landing major element quantification using SuperCam laser induced breakdown spectroscopy, Spectrochimica Acta Part B: Atomic Spectroscopy. (2021) 106347. https://doi.org/10.1016/j.sab.2021.106347.

[8] M. Gaft, L. Nagli, Y. Groisman, Plasma induced luminescence (PIL), Optical Materials. 34 (2011) 368–375. https://doi.org/10.1016/j.optmat.2011.05.024.

[9] M. Gaft, Y. Raichlin, F. Pelascini, G. Panzer, V. Motto Ros, Imaging rare-earth elements in minerals by laser-induced plasma spectroscopy: Molecular emission and plasma-induced

luminescence, Spectrochimica Acta Part B: Atomic Spectroscopy. 151 (2019) 12–19. https://doi.org/10.1016/j.sab.2018.11.003.
[10] E. Clavé, M. Gaft, V. Motto-Ros, C. Fabre, O. Forni, O. Beyssac, S. Maurice, R.C. Wiens, B. Bousquet, Extending the potential of plasma-induced luminescence spectroscopy, Spectrochimica Acta Part B: Atomic Spectroscopy. 177 (2021) 106111. https://doi.org/10.1016/j.sab.2021.106111.
[11] A. Nardecchia, A. de Juan, V. Motto-Ros, M. Gaft, L. Duponchel, Data fusion of LIBS and PIL hyperspectral imaging: Understanding the luminescence phenomenon of a complex mineral sample, Analytica Chimica Acta. 1192 (2022) 339368. https://doi.org/10.1016/j.aca.2021.339368.
[12] S.-B. Wen, X. Mao, R. Greif, R.E. Russo, Laser ablation induced vapor plume expansion into a background gas. II. Experimental analysis, Journal of Applied Physics. 101 (2007) 023115. https://doi.org/10.1063/1.2431085.
[13] A.D. Giacomo, M. Dell'Aglio, R. Gaudiuso, S. Amoruso, O.D. Pascale, Effects of the background environment on formation, evolution and emission spectra of laser-induced plasmas, (2012) 19. http://dx.doi.org/10.1016/j.sab.2012.10.003.
[14] A. De Giacomo, M. Dell'Aglio, O. De Pascale, R. Gaudiuso, V. Palleschi, C. Parigger, A. Woods, Plasma processes and emission spectra in laser induced plasmas: A point of view, Spectrochimica Acta Part B: Atomic Spectroscopy. 100 (2014) 180–188. https://doi.org/10.1016/j.sab.2014.08.013.
[15] J. Hermann, A. Lorusso, A. Perrone, F. Strafella, C. Dutouquet, B. Torralba, Simulation of emission spectra from nonuniform reactive laser-induced plasmas, Phys. Rev. E. 92 (2015) 053103. https://doi.org/10.1103/PhysRevE.92.053103.
[16] A. De Giacomo, J. Hermann, Laser-induced plasma emission: from atomic to molecular spectra, Appl. Phys. (2017) 18.
[17] Y. Iida, Effects of atmosphere on laser vaporization and excitation processes of solid samples, Spectrochimica Acta Part B: Atomic Spectroscopy. 45 (1990) 1353–1367. https://doi.org/10.1016/0584-8547(90)80188-O.
[18] A.K. Knight, N.L. Scherbarth, D.A. Cremers, M.J. Ferris, Characterization of Laser-Induced Breakdown Spectroscopy (LIBS) for Application to Space Exploration, Appl Spectrosc. 54 (2000) 331–340. https://doi.org/10.1366/0003702001949591.
[19] B. Sallé, D.A. Cremers, S. Maurice, R.C. Wiens, Laser-induced breakdown spectroscopy for space exploration applications: Influence of the ambient pressure on the calibration curves prepared from soil and clay samples, Spectrochimica Acta Part B: Atomic Spectroscopy. 60 (2005) 479–490. https://doi.org/10.1016/j.sab.2005.02.009.
[20] A. Effenberger, J. Scott, Effect of Atmospheric Conditions on LIBS Spectra, Sensors. 10 (2010) 4907–4925. https://doi.org/10.3390/s100504907.
[21] A. Cousin, O. Forni, S. Maurice, O. Gasnault, C. Fabre, V. Sautter, R.C. Wiens, J. Mazoyer, Laser induced breakdown spectroscopy library for the Martian environment, Spectrochimica Acta Part B: Atomic Spectroscopy. 66 (2011) 805–814. https://doi.org/10.1016/j.sab.2011.10.004.
[22] C.G. Parigger, Atomic and molecular emissions in laser-induced breakdown spectroscopy, Spectrochimica Acta Part B: Atomic Spectroscopy. 79–80 (2013) 4–16. https://doi.org/10.1016/j.sab.2012.11.012.
[23] J. Hermann, C. Gerhard, E. Axente, C. Dutouquet, Comparative investigation of laser ablation plumes in air and argon by analysis of spectral line shapes: Insights on calibration-free laser-induced breakdown spectroscopy, Spectrochimica Acta Part B: Atomic Spectroscopy. 100 (2014) 189–196. https://doi.org/10.1016/j.sab.2014.08.014.
[24] P.R. Mahaffy, C.R. Webster, S.K. Atreya, H. Franz, M. Wong, P.G. Conrad, D. Harpold, J.J. Jones, L.A. Leshin, H. Manning, T. Owen, R.O. Pepin, S. Squyres, M. Trainer, MSL Science Team, O. Kemppinen, N. Bridges, J.R. Johnson, M. Minitti, D. Cremers, J.F. Bell, L. Edgar, J. Farmer, A. Godber, M. Wadhwa, D. Wellington, I. McEwan, C. Newman, M. Richardson, A. Charpentier, L. Peret, P. King, J. Blank, G. Weigle, M. Schmidt, S. Li, R. Milliken, K. Robertson, V. Sun, M. Baker,

C. Edwards, B. Ehlmann, K. Farley, J. Griffes, J. Grotzinger, H. Miller, M. Newcombe, C. Pilorget, M. Rice, K. Siebach, K. Stack, E. Stolper, C. Brunet, V. Hipkin, R. Léveillé, G. Marchand, P.S. Sánchez, L. Favot, G. Cody, A. Steele, L. Flückiger, D. Lees, A. Nefian, M. Martin, M. Gailhanou, F. Westall, G. Israël, C. Agard, J. Baroukh, C. Donny, A. Gaboriaud, P. Guillemot, V. Lafaille, E. Lorigny, A. Paillet, R. Pérez, M. Saccoccio, C. Yana, C. Armiens-Aparicio, J.C. Rodríguez, I.C. Blázquez, F.G. Gómez, J. Gómez-Elvira, S. Hettrich, A.L. Malvitte, M.M. Jiménez, J. Martínez-Frías, J. Martín-Soler, F.J. Martín-Torres, A.M. Jurado, L. Mora-Sotomayor, G.M. Caro, S.N. López, V. Peinado-González, J. Pla-García, J.A.R. Manfredi, J.J. Romeral-Planelló, S.A.S. Fuentes, E.S. Martinez, J.T. Redondo, R. Urqui-O'Callaghan, M.-P.Z. Mier, S. Chipera, J.-L. Lacour, P. Mauchien, J.-B. Sirven, A. Fairén, A. Hayes, J. Joseph, R. Sullivan, P. Thomas, A. Dupont, A. Lundberg, N. Melikechi, A. Mezzacappa, J. DeMarines, D. Grinspoon, G. Reitz, B. Prats, E. Atlaskin, M. Genzer, A.-M. Harri, H. Haukka, H. Kahanpää, J. Kauhanen, O. Kemppinen, M. Paton, J. Polkko, W. Schmidt, T. Siili, C. Fabre, J. Wray, M.B. Wilhelm, F. Poitrasson, K. Patel, S. Gorevan, S. Indyk, G. Paulsen, S. Gupta, D. Bish, J. Schieber, B. Gondet, Y. Langevin, C. Geffroy, D. Baratoux, G. Berger, A. Cros, C. d'Uston, O. Forni, O. Gasnault, J. Lasue, Q.-M. Lee, S. Maurice, P.-Y. Meslin, E. Pallier, Y. Parot, P. Pinet, S. Schröder, M. Toplis, É. Lewin, W. Brunner, E. Heydari, C. Achilles, D. Oehler, B. Sutter, M. Cabane, D. Coscia, G. Israël, C. Szopa, G. Dromart, F. Robert, V. Sautter, S. Le Mouélic, N. Mangold, M. Nachon, A. Buch, F. Stalport, P. Coll, P. François, F. Raulin, S. Teinturier, J. Cameron, S. Clegg, A. Cousin, D. DeLapp, R. Dingler, R.S. Jackson, S. Johnstone, N. Lanza, C. Little, T. Nelson, R.C. Wiens, R.B. Williams, A. Jones, L. Kirkland, A. Treiman, B. Baker, B. Cantor, M. Caplinger, S. Davis, B. Duston, K. Edgett, D. Fay, C. Hardgrove, D. Harker, P. Herrera, E. Jensen, M.R. Kennedy, G. Krezoski, D. Krysak, L. Lipkaman, M. Malin, E. McCartney, S. McNair, B. Nixon, L. Posiolova, M. Ravine, A. Salamon, L. Saper, K. Stoiber, K. Supulver, J. Van Beek, T. Van Beek, R. Zimdar, K.L. French, K. Iagnemma, K. Miller, R. Summons, F. Goesmann, W. Goetz, S. Hviid, M. Johnson, M. Lefavor, E. Lyness, E. Breves, M.D. Dyar, C. Fassett, D.F. Blake, T. Bristow, D. DesMarais, L. Edwards, R. Haberle, T. Hoehler, J. Hollingsworth, M. Kahre, L. Keely, C. McKay, M.B. Wilhelm, L. Bleacher, W. Brinckerhoff, D. Choi, J.P. Dworkin, J. Eigenbrode, M. Floyd, C. Freissinet, J. Garvin, D. Glavin, A. Jones, D.K. Martin, A. McAdam, A. Pavlov, E. Raaen, M.D. Smith, J. Stern, F. Tan, M. Meyer, A. Posner, M. Voytek, R.C. Anderson, A. Aubrey, L.W. Beegle, A. Behar, D. Blaney, D. Brinza, F. Calef, L. Christensen, J.A. Crisp, L. DeFlores, B. Ehlmann, J. Feldman, S. Feldman, G. Flesch, J. Hurowitz, I. Jun, D. Keymeulen, J. Maki, M. Mischna, J.M. Morookian, T. Parker, B. Pavri, M. Schoppers, A. Sengstacken, J.J. Simmonds, N. Spanovich, M. de la T. Juarez, A.R. Vasavada, A. Yen, P.D. Archer, F. Cucinotta, D. Ming, R.V. Morris, P. Niles, E. Rampe, T. Nolan, M. Fisk, L. Radziemski, B. Barraclough, S. Bender, D. Berman, E.N. Dobrea, R. Tokar, D. Vaniman, R.M.E. Williams, A. Yingst, K. Lewis, T. Cleghorn, W. Huntress, G. Manhès, J. Hudgins, T. Olson, N. Stewart, P. Sarrazin, J. Grant, E. Vicenzi, S.A. Wilson, M. Bullock, B. Ehresmann, V. Hamilton, D. Hassler, J. Peterson, S. Rafkin, C. Zeitlin, F. Fedosov, D. Golovin, N. Karpushkina, A. Kozyrev, M. Litvak, A. Malakhov, I. Mitrofanov, M. Mokrousov, S. Nikiforov, V. Prokhorov, A. Sanin, V. Tretyakov, A. Varenikov, A. Vostrukhin, R. Kuzmin, B. Clark, M. Wolff, S. McLennan, O. Botta, D. Drake, K. Bean, M. Lemmon, S.P. Schwenzer, R.B. Anderson, K. Herkenhoff, E.M. Lee, R. Sucharski, M.Á. de P. Hernández, J.J.B. Ávalos, M. Ramos, M.-H. Kim, C. Malespin, I. Plante, J.-P. Muller, R. Navarro-González, R. Ewing, W. Boynton, R. Downs, M. Fitzgibbon, K. Harshman, S. Morrison, W. Dietrich, O. Kortmann, M. Palucis, D.Y. Sumner, A. Williams, G. Lugmair, M.A. Wilson, D. Rubin, B. Jakosky, T. Balic-Zunic, J. Frydenvang, J.K. Jensen, K. Kinch, A. Koefoed, M.B. Madsen, S.L.S. Stipp, N. Boyd, J.L. Campbell, R. Gellert, G. Perrett, I. Pradler, S. VanBommel, S. Jacob, S. Rowland, E. Atlaskin, H. Savijärvi, E. Boehm, S. Böttcher, S. Burmeister, J. Guo, J. Köhler, C.M. García, R. Mueller-Mellin, R. Wimmer-Schweingruber, J.C. Bridges, T. McConnochie, M. Benna, H. Bower, A. Brunner, H. Blau, T. Boucher, M. Carmosino, H. Elliott, D. Halleaux, N. Rennó, B. Elliott, J. Spray, L. Thompson, S. Gordon, H. Newsom, A. Ollila, J. Williams, P. Vasconcelos, J. Bentz, K. Nealson, R. Popa, L.C. Kah, J. Moersch, C. Tate, M. Day, G. Kocurek, B. Hallet, R. Sletten, R. Francis, E. McCullough, E. Cloutis, I.L. ten Kate, R. Kuzmin, R. Arvidson, A. Fraeman,

D. Scholes, S. Slavney, T. Stein, J. Ward, J. Berger, J.E. Moores, Abundance and Isotopic Composition of Gases in the Martian Atmosphere from the Curiosity Rover, Science. 341 (2013) 263–266. https://doi.org/10.1126/science.1237966.
[25] J. Blacic, D. Pettit, D. Cremers, N. Roessler, Laser-induced breakdown spectroscopy instrument for elemental analysis on planetary surfaces, in: LPI Technical Report 93-02, 1993.
[26] R.C. Wiens, R.E. Arvidson, D.A. Cremers, M.J. Ferris, J.D. Blacic, F.P. Seelos, K.S. Deal, Combined remote mineralogical and elemental identification from rovers: Field and laboratory tests using reflectance and laser-induced breakdown spectroscopy: identification using reflectance and LIBS, J.-Geophys.-Res. 107 (2002) FIDO 3-1-FIDO 3-14. https://doi.org/10.1029/2000JE001439.
[27] R. Brennetot, J.L. Lacour, E. Vors, A. Rivoallan, D. Vailhen, S. Maurice, Mars Analysis by Laser-Induced Breakdown Spectroscopy (MALIS): Influence of Mars Atmosphere on Plasma Emission and Study of Factors Influencing Plasma Emission with the Use of Doehlert Designs, Appl Spectrosc. 57 (2003) 744–752. https://doi.org/10.1366/000370203322102816.
[28] F. Colao, R. Fantoni, V. Lazic, A. Paolini, F. Fabbri, G.G. Ori, L. Marinangeli, A. Baliva, Investigation of LIBS feasibility for in situ planetary exploration: An analysis on Martian rock analogues, Planetary and Space Science. 52 (2004) 117–123. https://doi.org/10.1016/j.pss.2003.08.012.
[29] S. Maurice, S.M. Clegg, R.C. Wiens, O. Gasnault, W. Rapin, O. Forni, A. Cousin, V. Sautter, N. Mangold, L. Le Deit, M. Nachon, R.B. Anderson, N.L. Lanza, C. Fabre, V. Payré, J. Lasue, P.-Y. Meslin, R.J. Léveillé, B.L. Barraclough, P. Beck, S.C. Bender, G. Berger, J.C. Bridges, N.T. Bridges, G. Dromart, M.D. Dyar, R. Francis, J. Frydenvang, B. Gondet, B.L. Ehlmann, K.E. Herkenhoff, J.R. Johnson, Y. Langevin, M.B. Madsen, N. Melikechi, J.-L. Lacour, S. Le Mouélic, E. Lewin, H.E. Newsom, A.M. Ollila, P. Pinet, S. Schröder, J.-B. Sirven, R.L. Tokar, M.J. Toplis, C. d'Uston, D.T. Vaniman, A.R. Vasavada, ChemCam activities and discoveries during the nominal mission of the Mars Science Laboratory in Gale crater, Mars, J. Anal. At. Spectrom. 31 (2016) 863–889. https://doi.org/10.1039/C5JA00417A.
[30] P.-Y. Meslin, A. Cousin, J.G. Blank, F.M. McCubbin, O. Gasnault, H. Newsom, N. Mangold, S. Schröder, R.C. Wiens, N. Ames, M. Field, Calibration of the fluorine, chlorine and hydrogen content of apatites with the ChemCan LIBS instrument, in: 2016: p. 1703. https://ntrs.nasa.gov/api/citations/20160003503/downloads/20160003503.pdf.
[31] O. Forni, M. Gaft, M.J. Toplis, S.M. Clegg, S. Maurice, R.C. Wiens, N. Mangold, O. Gasnault, V. Sautter, S.L. Mouélic, P.-Y. Meslin, M. Nachon, R.E. McInroy, A.M. Ollila, A. Cousin, J.C. Bridges, N.L. Lanza, M.D. Dyar, First detection of fluorine on Mars: Implications for Gale Crater's geochemistry, Geophysical Research Letters. 42 (2015) 1020–1028. https://doi.org/10.1002/2014GL062742.
[32] M. Gaft, L. Nagli, N. Eliezer, Y. Groisman, O. Forni, Elemental analysis of halogens using molecular emission by laser-induced breakdown spectroscopy in air, Spectrochimica Acta Part B: Atomic Spectroscopy. 98 (2014) 39–47. https://doi.org/10.1016/j.sab.2014.05.011.
[33] D.S. Vogt, S. Schröder, K. Rammelkamp, P.B. Hansen, S. Kubitza, H.-W. Hübers, CaCl and CaF emission in LIBS under simulated martian conditions, Icarus. 335 (2020) 113393. https://doi.org/10.1016/j.icarus.2019.113393.
[34] D.S. Vogt, K. Rammelkamp, S. Schröder, H.W. Hübers, Molecular emission in laser-induced breakdown spectroscopy: An investigation of its suitability for chlorine quantification on Mars, Icarus. 302 (2018) 470–482. https://doi.org/10.1016/j.icarus.2017.12.006.
[35] T. Delgado, L. García-Gómez, L.M. Cabalín, J.J. Laserna, Investigation on the origin of molecular emissions in laser-induced breakdown spectroscopy under Mars-like atmospheric conditions of isotope-labeled compounds of interest in astrobiology, Spectrochimica Acta Part B: Atomic Spectroscopy. 179 (2021) 106114. https://doi.org/10.1016/j.sab.2021.106114.
[36] L.J. Fernández-Menéndez, C. Méndez-López, C. Alvarez-Llamas, C. González-Gago, J. Pisonero, N. Bordel, Spatio-temporal distribution of atomic and molecular excited species in Laser-Induced Breakdown Spectroscopy: Potential implications on the determination of halogens,

Spectrochimica Acta Part B: Atomic Spectroscopy. 168 (2020) 105848. https://doi.org/10.1016/j.sab.2020.105848.
[37] D.S. Vogt, S. Schröder, S. Frohmann, P.B. Hansen, F. Seel, M. Gensch, H.-W. Hübers, Spatiotemporal characterization of the laser-induced plasma plume in simulated Martian conditions, Spectrochimica Acta Part B: Atomic Spectroscopy. 187 (2022) 106326. https://doi.org/10.1016/j.sab.2021.106326.
[38] T. Delgado, J.M. Vadillo, J.J. Laserna, Pressure Effects in Laser-Induced Plasmas of Trinitrotoluene and Pyrene by Laser-Induced Breakdown Spectroscopy (LIBS), Appl Spectrosc. 68 (2014) 33–38. https://doi.org/10.1366/13-07164.
[39] G. Alombert-Goget, H. Li, Y. Guyot, A. Brenier, K. Lebbou, Luminescence and coloration of undoped and Ti-doped sapphire crystals grown by Czochralski technique, Journal of Luminescence. 169 (2016) 516–519. https://doi.org/10.1016/j.jlumin.2015.02.001.
[40] J. Davidson, M. Wadhwa, R.L. Hervig, A. Stephant, Water on Mars: Insights from apatite in regolith breccia Northwest Africa 7034, Earth and Planetary Science Letters. 552 (2020) 116597. https://doi.org/10.1016/j.epsl.2020.116597.
[41] R.F. Marks, H.S. Schweda, R.A. Gottscho, The orange arc bands of CaO. Analysis of a D,d 1,3Δ–a 3Π system, J. Chern. Phys. 76 (1982) 4689. https://doi.org/10.1063/1.442784.
[42] M. Gaft, R. Reisfeld, G. Panczer, Modern Luminescence Spectroscopy of minerals and materials, 2015.
[43] A. Fau, O. Beyssac, M. Gauthier, G. Panczer, O. Gasnault, P.-Y. Meslin, S. Bernard, S. Maurice, O. Forni, J.-C. Boulliard, Time-resolved Raman and luminescence spectroscopy of synthetic REE-doped hydroxylapatites and natural apatites, Msam. (2021). https://doi.org/10.2138/am-2022-8006.
[44] NIST LIBS Database, (n.d.). https://physics.nist.gov/PhysRefData/ASD/LIBS/libs-form.html.
[45] J. Zhang, Q. Guo, L. Liao, Y. Wang, M. He, H. Ye, L. Mei, H. Liu, T. Zhou, B. Ma, Structure and luminescence properties of $La_6Ba_4(SiO_4)_6F_2:Dy^{3+}$ phosphor with apatite structure, RSC Adv. 8 (2018) 38883–38890. https://doi.org/10.1039/C8RA08324J.
[46] S. Romppanen, H. Häkkänen, S. Kaski, Laser-induced time-resolved luminescence in analysis of rare earth elements in apatite and calcite, Journal of Luminescence. 233 (2021) 117929. https://doi.org/10.1016/j.jlumin.2021.117929.

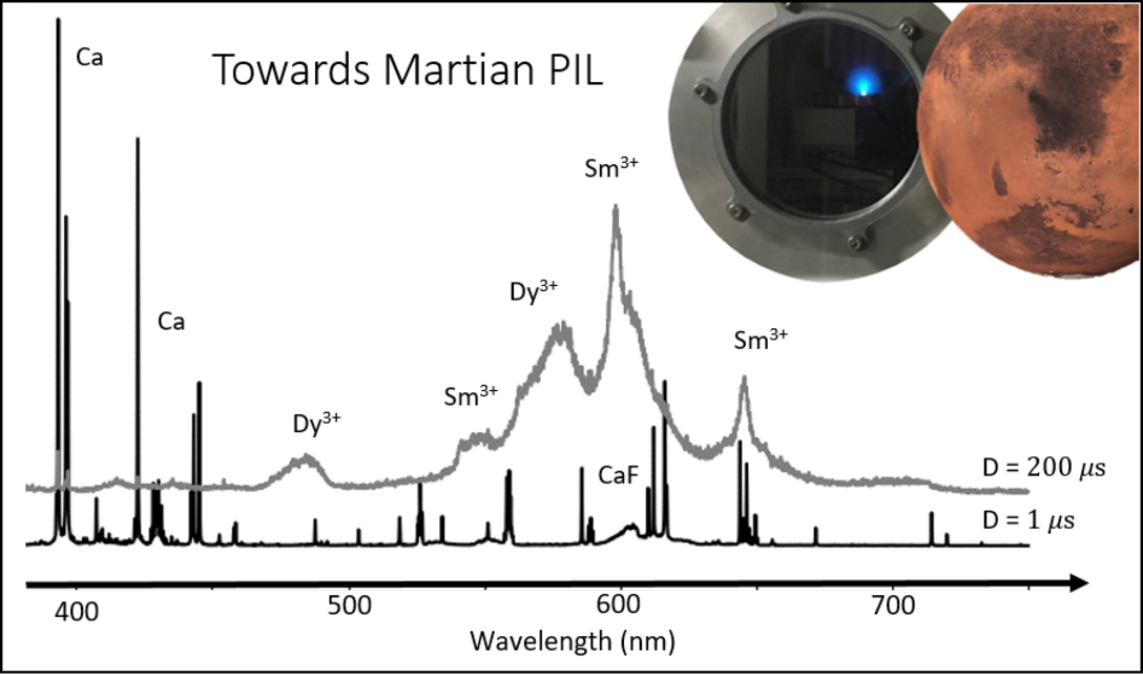
Towards Martian PIL
Ca
Ca
Dy3+
Sm3+
Dy3+
Sm3+
CaF
Sm3+
D = 200 μs
D = 1 μs
400
500
600
700
Wavelength (nm)